Powder Technology 408 (2022) 117790

Contents lists available at ScienceDirect

Powder Technology

journal homepage: www.journals.elsevier.com/powder-technology

Discrete element simulation of powder flow in revolution powder analyser: Effects of shape factor, friction and adhesion

L. Dai [a,*], Y.R. Chan [b], G. Vastola [a], Y.W. Zhang [a,*]

[a] Institute of High Performance Computing, Agency for Science, Technology and Research (A*STAR), Singapore
[b] Advanced Remanufacturing and Technology Centre, Agency for Science, Technology and Research (A*STAR), Singapore

HIGHLIGHTS

- DEM powder flow models with realistic powder size and shape distributions.
- Performed DEM simulations to study powder flow profiles and avalanche phenomena.
- Examined and identified the effects of system factors for reliable RPA measurements.
- Extracted the rolling COF and adhesion energy by including powder non-sphericity.

GRAPHICAL ABSTRACT

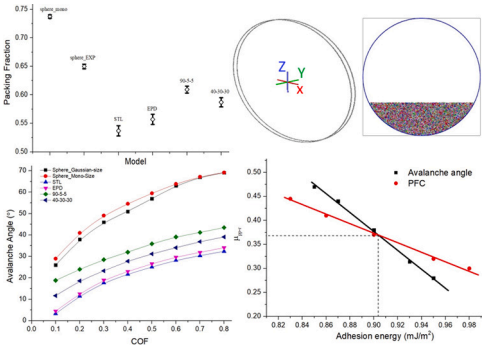

ARTICLE INFO

Keywords:
DEM
Powder
Revolutionary powder analyser
Flow
Friction
Avalanche

ABSTRACT

Through discrete element method (DEM) simulations in Revolution Powder Analyser (RPA), we found a strong correlation between the static powder bed packing density and the avalanche flow. A wider powder size distribution and a higher fraction of non-spherical powders caused larger misfits in the static packing of powders, and thereby enhanced the powder mobility during revolution, leading to an earlier avalanche. It performs a gradual avalanche under low friction, and an abrupt avalanche under high friction. The rolling motion of non-spherical powders was found to cause an instantaneous disturbance to the flow of neighbouring powders. It was also found that other factors, such as the filling degree, drum rotation speed and inter-powder adhesion, can also influence the measurement results and hence they must be controlled or standardized in order to achieve reliable and consistent measurements. Furthermore, based on the experimental measurements of avalanche angle and packing fraction, we extracted the intrinsic powder friction coefficient and adhesion energy.

1. Introduction

Rotating drum has a long history of industrial applications for different purposes, such as mixing, segregating, grinding, drying, in various industries including concrete, food, pharmaceutics, and metallurgy [1]. In recent decades, with the development of additive manufacturing, the rotating drum has become an instrument of powder characterization, named Revolution Powder Analyser (RPA). During

* Corresponding authors.
E-mail addresses: dail@ihpc.a-star.edu.sg (L. Dai), zhangyw@ihpc.a-star.edu.sg (Y.W. Zhang).

https://doi.org/10.1016/j.powtec.2022.117790
Received 12 April 2022; Received in revised form 17 July 2022; Accepted 26 July 2022
Available online 29 July 2022

drum rotation, the fine powders are elevated and perform characteristic flows which are dictated by the working conditions and their intrinsic properties [2,3]. An impressive theoretical work on the powder flow was reported in 2001 by Mellmann [4], who defined seven powder flow regimes based on different physical and working conditions. More specifically, after being elevated to a certain height under a relatively slow drum rotation, the powders will slide down in an avalanche manner. The avalanche angle (AA), which is defined as the angle between the slope of the powder bed surface and the horizontal plane at the onset of avalanche, is an important feature which highly depends on the powder geometry (size, shape, etc.) and mechanics (friction, restitution, adhesion, etc.) [5]. The powder geometrical and mechanical properties play a key role for powder bed packing [6] during the additive manufacturing process, which makes RPA a popular means of powder characterizations and has attracted abundant interest of research activities [5,7–11].

Liu et al. [12] carried out RPA experiments of spherical glass powders with diameter of 3 mm or 5 mm, in rotation drums of diameter 200 mm, 300 mm or 500 mm. They observed that the slope of the powder bed surface would decrease after the occurrence of avalanche, and defined the upper angle of repose (AOR) (same as AA) and lower AOR as the powder bed surface slope at the onset and end of avalanche, respectively. Both AORs increased with higher ratio of powder diameter vs drum diameter (d/D), but were little affected by the filling degree (20%–40% volume occupation by powder in the drum) and drum rotation speed (below 1 rpm). The two AORs were correlated in a way that the upper AOR was always slightly higher than the lower AOR and an empirical mathematical formula was proposed. These characteristics were shown to be applicable to other materials in powder form (limestone, gravel, metal oxide, sand, etc.) and a wide coverage of d/D ratios. Chou and Hsiau [13] immersed the glass powder in water and water-glycerol to introduce viscosity among powders, which led to intensified avalanche. In a later work [14], they claimed that friction was critically important for the powder flow and a higher friction led to a higher AA. They defined three types of powder flow: sliding domain, friction domain and potential energy domain, during the rotational elevation. Similar to viscosity, the adhesion between powders was found to induce abrupt avalanche by means of jamming powders during elevation, as reported by Yang et al. [15]. A series of RPA studies on non-spherical sand powder were done by Chen and Yang et al. [9,16–18]. They reported that non-spherical powder presented a continuous slight motion of re-locating during elevating which led to compaction or dilatancy of the powder bed packing volume. Non-spherical powder was more likely to exhibit abrupt avalanche, while spherical powder would prefer a gradual avalanche [9]. The powder shape effect was also studied in Zhao's experiment [11] in which good flowability was found to be highly dependent on the high sphericity of individual powders.

Compared to experiments, discrete element modelling (DEM) shows its power of being able to simulate and measure physical quantities that are often inaccessible to experiments [19], and have proven of being able to reproduce various physical phenomena of powder mechanics and dynamics [20–23]. Simulations by DEM on mixing or segregation of powders by means of drum rotational percolation were validated by experiments [5,19,24–31]. Yang et al. [32] modelled 3-mm-diameter polymer powder with 35% filling degree in a 100-mm-diameter drum rotating at 10–65 rpm. Their measured dynamic AOR and spatial flow profile were in good agreement with experimental measurements. In a later work by Yang et al. [33] the drum rotation rate and powder-wall friction were tuned to reproduce 6 flow regimes defined by Mellmann [4]. Combarros et al. [24] showed that powder rolling motion became more dominant to the powder flow when sliding friction was strong. Besides the flow, the avalanche was also a special interest of study. As predicted in DEM simulation, the AA could be decreased by a lower filling degree or a slower drum rotation speed [5]. Han et al. [10] reported that the quantity of powders participating in avalanche could increase, then stabilize, and finally decrease during the avalanche process. The external perturbation of vibration was found to be able to trigger an early avalanche due to enhanced kinetics, as reported by Salinas et al. [34]. Kasper et al. [35] simulated the avalanche flow by including the effect of adhesion between powders and their simulations were supported by experiments on flow pattern and AA measurements.

A challenge for DEM is the modelling of non-spherical powders due to the difficulties in handling the contact and rolling dynamics [36–38]. The clump method, i.e. clumping of multiple spheres, has been widely accepted as the most reliable means of representing a shape which is non-spherical, and has been adopted in many works [3,20,39–43]. Pachon-Morales et al. [44] reported an interesting work with a combination of experiment and DEM to study the powder flow pattern in the rotating drum, in which the clump method was used to reproduce the flow characteristics of non-spherical powders in their experiment. However, most studies modelled only one type of non-spherical shape powder. In reality, a combination of various shaped powders, including spheres and different shapes of non-spheres, are present. It is also noted that most of previous studies focused on the powder at the millimetre-size scale, while the modern additive manufacturing technologies are based on powder at the scale of the micron, for which research works are still far from sufficient [5]. Furthermore, in RPA, the powder flow and avalanche may be simultaneously dependent on many factors, such as size, shape, adhesion, filling degree, and drum rotation speed, etc. Therefore, an in-depth understanding on the inter-dependence is important and necessary.

Recently, coarse grain (CG) models have been developed by representing several powders by a big pseudo powder so as to approach the experimental size scale [45–47]. To set up a proper CG model, one needs to understand the individual powder behavior at the DEM level so as to make the CG predictions on the powder packing and flowability consistent with the DEM results. Thus, systematic DEM studies are able to provide a useful reference for developing coarsening scheme.

Here, we report our DEM study on RPA by focusing on the effects of powder shape factor, friction and adhesion. Through analysing the velocity profiles and avalanche patterns, we show that the powder shape factor plays an important role in the packing fraction, mobility and avalanche during revolution. Friction was also found to affect powder flow during revolution with a gradual avalanche under a low friction, and an abrupt avalanche under a high friction. It was also found that other factors, such as the filling degree, drum rotation speed and inter-powder adhesion, must be controlled properly in order to make a reliable measurement of avalanche flow. Furthermore, based on the experimental measurements, we extracted the intrinsic powder friction coefficient and adhesion energy. Our work provides an in-depth understanding on powder flow and presents a viable approach to characterize the friction and adhesion properties of powder using RPA devices.

2. Methodology

2.1. Experiment work

Inconel 718 [48–50] powder, directly purchased from GE Additive [51], was used for the RPA tests. The powders were firstly baked at 80 °C for 24 h, then Malvern Morphologi G3 machine (Fig. 1a) was used to measure the shape and size of the powders.

The powder shape was characterized by the HS circularity [52] and Aspect Ratio [53]. The HS circularity is computed by the perimeter, with definition as Eq. (1):

$$\text{HS circularity} = (\text{perimeter}/\text{perimeter of an equivalent area circle})^2 \quad (1)$$

The HS circularity has a value of 1 for a perfect sphere and ~0 for a thin needle shape. In our measurement as plotted in Fig. 1(d-1), the HS circularity values were 0.95 or above for about 90% of the powders, and these powders were taken as a spherical shape in DEM simulation.

Unlike HS circularity, the Aspect Ratio is based on the body length, and computed by Eq. (2):

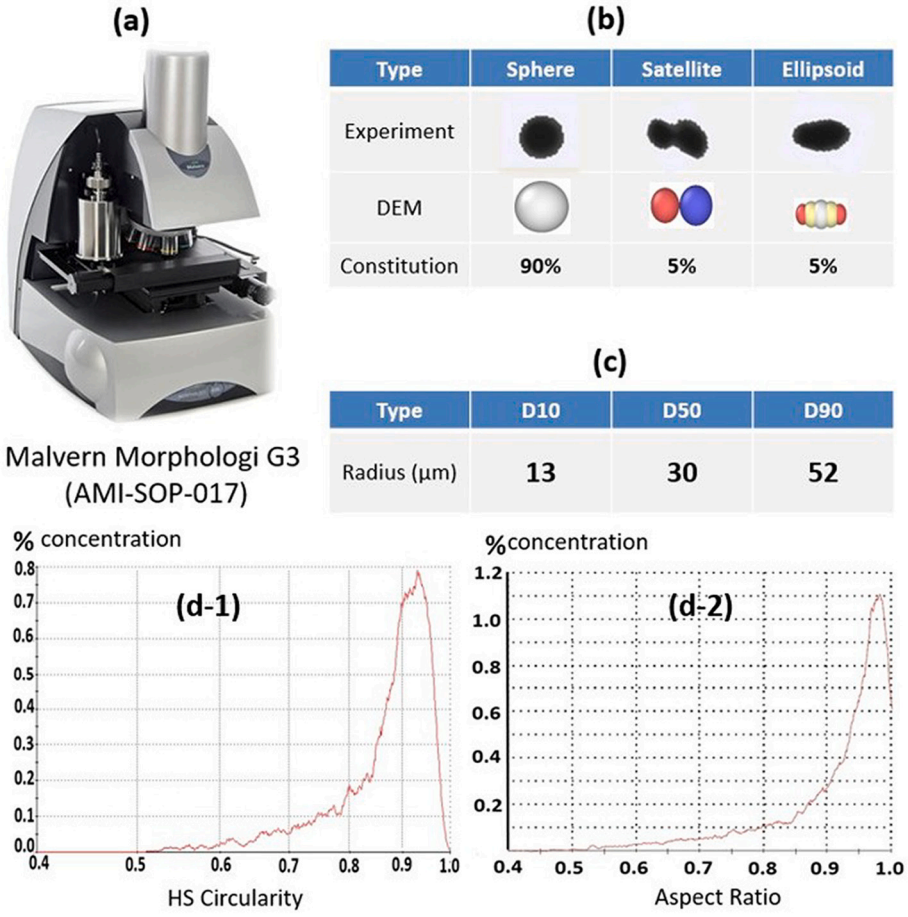

Fig. 1. (a) Malvern Morphologi G3 machine for measuring the size and shape following the AMI-SOP-017 procedure.
(b) Results from powder shape measurement and scheme taken for powder shape modelling in DEM.
(c) Measured size distribution as D10, D50 and D90 for spherical powders.
(d-1) Concentration plot for HS Circularity.
(d-2) Concentration plot for Aspect Ratio.

$$\text{Aspect Ratio} = (\text{Width}/\text{Length}) \tag{2}$$

The definition of Length and Width was given in Appendix. Similar to the case of HS circularity, the value of Aspect Ratio increases from 0 to 1 for more sphere-like shapes. Fig. 1(d-2) plotted the concentration curve of Aspect Ratio, which showed highly consistent characteristics with HS circularity on the individual powder shapes.

The remaining non-spherical powders could be roughly categorized into two different groups, namely, Satellite (STL) and Ellipsoid (EPD), with each one accounting for about 5% of the constituent (Fig. 1b). It is noted that since it was difficult to accurately identify every single powder, such shape categorization could be considered as an overall estimation.

Besides HS Circularity and Aspect Ratio, there are quite a few means of definition to the particle shape [54,55], and this topic was well reviewed by Mitchell and Soga [56] and Roussillon et al. [57]. Roussillon et al. [57] compared different means of measurement on particle shape, in which the HS circularity provides a satisfactory description of particle shape by characterizing the perimeter. In our experiment, HS circularity and Aspect Ratio data, which were characterized by perimeter and length respectively, well agreed with each other on the powder shape characterizations. Therefore, it was sufficient for our DEM model setup.

The powder size was measured as the diameter of the spherical powders, and the size distribution (D10, D50 and D90) is shown in Fig. 1c.

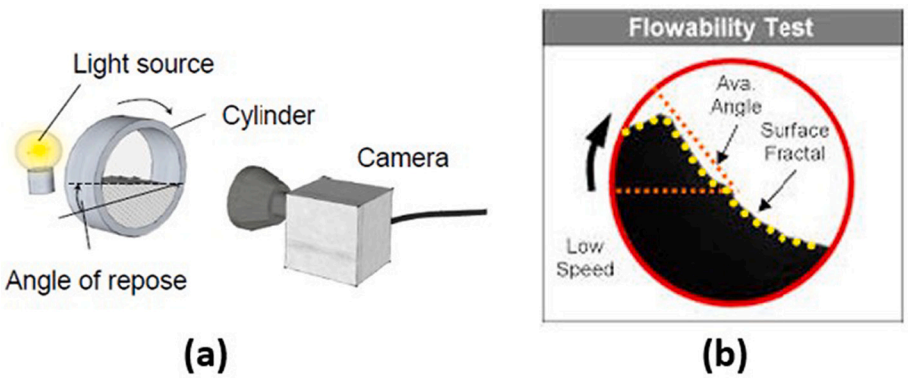

Fig. 2. (a) Schematic view of RPA operation.
(b) Schematic view of powder bed surface and avalanche angle.

Fig. 2a presents the device for RPA testing, in which the AOR for the powder bed is indicated. The drum had an inner diameter of 30 mm and rotated at a constant rate as 0.3 rpm during operation. This rotation speed is recommended by the RPA testing procedure [58], and thus used in our testing and DEM simulations. The avalanche angle is schematically illustrated in Fig. 2b. The RPA revolutionary elevating process was repeated 5 times from which a mean-valued output data was obtained.

2.2. DEM model

A DEM simulation package was developed in-house in C++ language to model, run and post-process the RPA simulations. Firstly, we set up the model schemes for the three different powder types. As shown in Fig. 1b, a sphere was used to represent a spherical powder. We set up 12 types of spheres with distinct diameters from 10 μm to 60 μm, with a Gaussian distribution of diameter based on D10, D50 and D90 (Fig. 1c). A non-spherical powder, i.e., STL or EPD, was modelled as clump of multiple spheres and treated as one rigid body. The STL shape was modelled as a clump of two glued spheres (Fig. 1b). The diameter of each member sphere was randomly picked from the Gaussian distribution of 12 values of diameter. Thus, there were totally 72 sub-types of STL powders with a combination of different size of member spheres. An EPD powder was modelled as five clumped spheres, which were located symmetrically and partially overlapping with neighbouring spheres (Fig. 1b). Following experimental observation, we set up two sub-types of EPD powders with distinct diameters in this sequence: 30 μm–34 μm-38 μm-34 μm-30 μm and 18 μm–22 μm-26 μm-22 μm-18 μm for the constituent spheres from left to right (Fig. 1b).

The drum was modelled as a thin cylinder with axis directions as shown in Fig. 3h. The drum thickness was 0.3 mm along the Y axis and periodic boundary conditions were applied so that it could represent a long length drum. In the XZ plane, the diameter of the drum vertical circle was 6 mm, which is 1/5 of the experimental size. It has been shown [22] that the DEM results are consistent with experiments when the value of drum/powder diameter (D/d) is larger than 25. In our model, D/d ranges from 100 to 600. Furthermore, we performed additional simulations with different sized drums. A 15 mm-diameter drum was built up to simulate rotational elevation processes, for which we predicted consistent values of static packing fraction and AA as the case of a 6 mm-diameter drum. However, the computational cost increased at least 50 times, which is too much to be affordable for practical simulations. Besides the drum diameter, we also validated the drum thickness via building up a drum model with 0.6 mm thickness, for which we also predicted consistent values of static packing fraction and AA. A summary of the simulation results is given in Table 2. Therefore, we believe that our choice of drum diameter and thickness was suitable.

The powder-powder interaction was described by Renzo's method [59,60] for linear mechanics and Ai's method [61] for rolling dynamics, for which the equations and parameters have been described in our previous work [62]. When a powder contacted with the drum inner wall, the wall was treated as a powder with an infinitely large radius. The key parameters for the dynamic simulation are shown in Table 1. The values of Poisson's ratio and coefficient of restitution were referenced from Combarros' literature [24]. Friction played an import role and introduced the following coefficients of friction: $\mu_{pp\text{-}s}$ and $\mu_{pp\text{-}r}$ for sliding and rolling between two powders, and $\mu_{pw\text{-}s}$ and $\mu_{pw\text{-}r}$ for sliding and rolling between powder and wall. In our previous Hall Flow simulation [62], we validated $\mu_{pw\text{-}s} = \mu_{pw\text{-}r} = 0.05$. Here, our experimental work used the same batch of powders and the inner surface of drum was made of hard and smooth metal similar to the inner surface of Hall Flowmeter. Thus,

Table 1
Parameters used in the DEM model.

Parameter	Value
Material	Inconel718
Young's modulus (GPa)	205
Powder density (kg/m^3)	8192
Poisson ratio	0.22
Coefficient of Restitution	0.75
$\mu_{pw\text{-}s}$	0.05
$\mu_{pw\text{-}r}$	0.05
Time step	1 μs

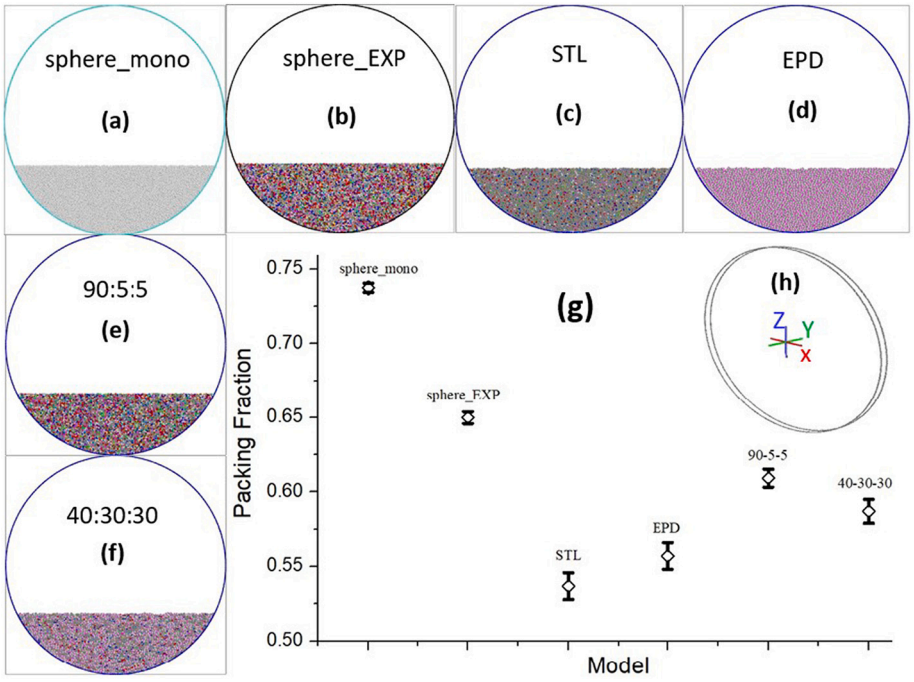

Fig. 3. Front view of powder bed with different types of powders. (a) Sphere_mono, (b) sphere_EXP, (c) STL, (d) EPD, (c) a mix ratio of 90:5:5 for sphere:STL:EPD, and (d) a mix ratio of 40:30:30 for sphere:STL:EPD. (g) Packing fraction of powder bed in each model. (h) 3D view for the drum. The powder and member spheres are coloured according to their diameters.

we adopted the validated constant value as 0.05 for both $\mu_{pw\text{-}s}$ and $\mu_{pw\text{-}r}$. The values for $\mu_{pp\text{-}s}$ and $\mu_{pp\text{-}r}$ will be tuned for parametric study later in this report.

For the non-spherical powders, the interaction force was computed based on the constituent spheres, and then summed up for the clumped body. The dynamics, i.e., linear and rolling movements, were firstly updated on the clumped body, before updating the position of each constituent sphere during each time step. The rolling motion was applied as rotation around its mass centre. The momentum of inertia was calculated by means of space integration and stored for each individual powder.

Here, we set up 6 models of powder bed with different combinations of powder types: spheres with mono-diameter as 30 μm (sphere_mono, Fig. 3a), spheres with experimental Gaussian distribution of diameters between 10 μm and 60 μm (sphere_EXP, Fig. 3b), pure STL (Fig. 3c), pure EPD (Fig. 3d), a mixture of three shapes with concentration as 90%, 5%, and 5%, for sphere, STL and EPR, respectively (90:5:5, Fig. 3e) in accordance with the experiments, and a mixture of three shapes with concentration as 40%, 30%, and 30%, for sphere, STL and EPR, respectively (40:30:30, Fig. 3f) for comparison.

Fig. 3g shows the static packing fraction (PF) for the six models as Fig. 3(a)–(f). The PF is defined as the volume fraction occupied by the individual powders with respect to the volume enclosed by the outer surface of the powder bed. It can be seen that PF is highly dependent on the powder shape and size distribution. The highest PF = 0.73 belongs to the model sphere_mono due to fewer voids among identical spheres. Our PF values for monodisperse powders in the drum, which are 0.73, are higher than those on a flat surface, which are about 0.64 [6,63]. Due to the gravitation force and the supporting force from the drum wall, powders experience a tangential force along the wall surface to drive the powders to move downward. As a result, the powders experience a squeezing force along the tangential direction of the drum surface. This squeezing force drives the powders to more likely form a closely packed powder bed, which in turn provides a good base for a high-density packing above. In sphere_EXP model, the misfit among different sized spheres created more voids, lowering PF to 0.64. The effect of non-spherical shape was more complex. The STL powder had 72 sub-types with a random combination of two-member spheres with random size, and many misfit voids were spotted among the different sized powders, leading to the lowest PF (=0.53). Compared to STL, the EPD powder had a symmetrical geometry, slightly enhancing PF to 0.56. With a mixture of different sizes and shapes, the PFs of 90-5-5 (=0.61) and 40–30-30 (=0.58) were at a medium range, between which the PF of 90-5-5 was slightly higher due to the higher ratio of spherical powder in the constituency.

Table 2
Static packing fraction (PF) and avalanche angle (AA) for models with different drum size.

	Static PF (COF = 0.1)		AA (COF = 0.1)		AA (COF = 0.8)	
model	Sphere_EXP	90-5-5	Sphere_EXP	90-5-5	Sphere_EXP	90-5-5
6 mm-drum (0.3 mm-thick)	0.64	0.61	38°	18.8°	70.5°	43.1°
15 mm-drum (0.3 mm-thick)	0.64	0.61	38.0°	18.8°	70.4°	43.0°
6 mm-drum (0.6 mm-thick)	0.64	0.61	38.1°	18.7°	70.5°	43.0°

To start the simulation, the powders were firstly poured into the drum and equilibrated for 10 s to form an equilibrated powder bed which occupied 28% of the free volume inside the drum. The front views for the static powder beds within the drum are presented in Fig. 3(a)–(f).

Afterwards, a constant clockwise angular velocity was assigned to all the powders, which was equivalent to the experimental drum rotation speed of 0.3 rpm. During each time step, the constant angular velocity was firstly applied to update the position of individual powders, and then the interaction forces were computed and the dynamics was updated. The drum rotation was carried out until a consistent powder flow/avalanche pattern was reached. With a time step of 1 μs for dynamic updating, each revolutionary simulation generally required 30 to 60 million time steps, i.e. 30–60 s of simulation time, which corresponded to a few days of computational time on a 64-CPU supercomputer cluster.

3. Results and discussion

3.1. Spherical powder

Firstly, we carried out the RPA simulation with sphere_mono, whose static powder bed model is shown in Fig. 3a. Here, we defined a notation as inclusive velocity, which was computed by summing up the sliding and rolling velocities (excluding the constant angular velocity induced by the drum rotation) of individual powder, in which the rolling velocity was converted into sliding term by multiplying the rolling radius to the mass centre. Then we plotted these inclusive velocities by color to present their magnitudes along certain axis directions. Three RPA simulations with different COF settings were carried out, in which the COF was taken as the same value for both $\mu_{pp\text{-}s}$ and $\mu_{pp\text{-}r}$, as 0.1, 0.4 and 0.8. For example, Fig. 4 shows such profiles of inclusive velocities along the –X axis ($\boldsymbol{V_x}$), in which the simulations with different COF settings were presented by row as (a), (b) and (c). In each row, the value of COF was presented, followed by a color bar to indicate the scale of velocity magnitude, and three profile plots in time sequential snapshots, as the instants of early stage (chart-1), right before the onset of avalanche (chart-2), and the final equilibrated avalanche flow (chart-3). The profiles with the format along –Z axis ($\boldsymbol{V_z}$) are shown in Fig. 5.

In Fig. 4, the $\boldsymbol{V_x}$ profile clearly demonstrates the COF effect. When

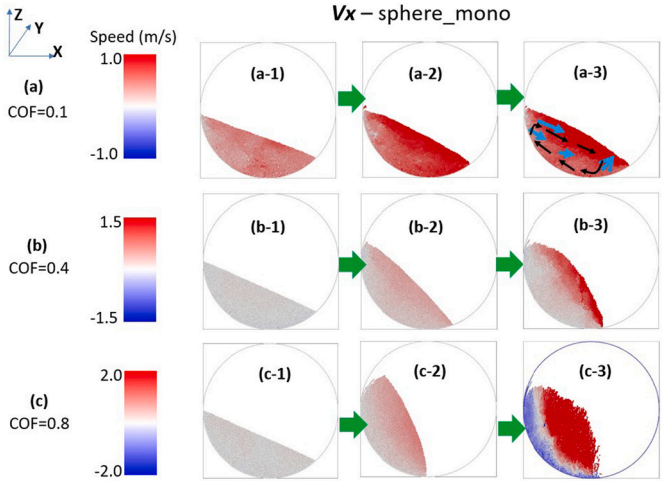

Fig. 4. Snapshots of $\boldsymbol{V_x}$ for sphere_mono with different friction settings. The velocity is positive when its direction is along the forward direction axis, and vice versa. In (a-3), the cyan arrows stand for the direction of inclusive velocities summed up from the sliding and rolling dynamics of powders, and are turned into dark arrows after adding the constant angular velocity from the drum rotation. (For interpretation of the references to color in this figure legend, the reader is referred to the web version of this article.)

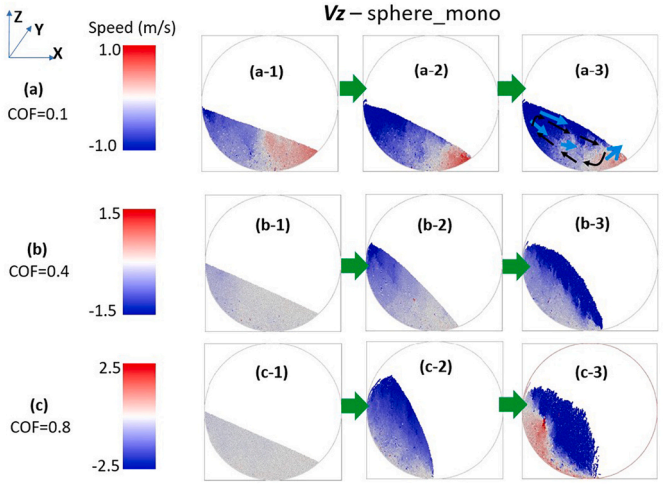

Fig. 5. Snapshots of V_z for sphere_mono with different friction settings. The velocity is positive when its direction is along the forward direction axis, and vice versa. In (a-3), the cyan arrows stand for the direction of inclusive velocities summed up from the sliding and rolling dynamics of powders, and are turned into dark arrows after adding the constant angular velocity from the drum rotation. (For interpretation of the references to color in this figure legend, the reader is referred to the web version of this article.)

COF = 0.1 (Fig. 4a), after an early stage of elevation (Fig. 4(a-1)), the powders began to avalanche into a gradual flow (Fig. 4(a-2, 3)). During avalanche, the powder located at the left-top of the powder bed started to slide down under gravity force. The inclusive velocities were higher at the powder bed surface, and gradually decreased for powders near the drum inner surface. In Fig. 4(a-3), the directions of the inclusive velocities are shown as the cyan arrows. Meanwhile, after adding the constant drum rotational angular velocity, the powders formed an enclosed flow circle: powders slid downward along the powder bed surface, and were being pushed up by the drum rotation along the wall inner surface, shown as the dark arrows. During avalanche flow, the powder bed surface was expanded to form a hood surface, due to the squeezing between flowing powders. The observed circulating flow and the hood surface were in agreement in previous experimental observations [9,13]. The AA, which is defined as the dynamic AOR [3,64] (Fig. 4 (a-2)), was measured as 41° (plot in Fig. 8). It is noted that the dynamic AOR from rotating drum measurements is usually 3 to 10° less than the static AOR [65]. Moreover, a representative dynamic AOR was previously defined as the average of the upper and the lower AOR in the drum [66]. Here, we used the upper AOR instead, in accordance with the experimental measurement (Fig. 2b). Meanwhile, the AA computed based on the lower half of the powder bed surface was slightly higher, at about 46°. This difference was attributed to the effect of powder-wall friction [67].

With higher friction as COF = 0.4 (Fig. 4b), the powders stuck with each other more tightly so as to hinder the powder flow and postpone the avalanche. This led to a higher AA (=59°, model view in Fig. 4(b-2) and plot in Fig. 8) because the powders needed to accumulate more potential energy to trigger the avalanche. During avalanche, the powder mobility was intensified, and the powder bead hood surface was further expanded accordingly, as shown in Fig. 4(b-3).

When COF = 0.8 (Fig. 4c), the highly enhanced powder-powder affinity further increased the AA to 70° (model view in Fig. 4(c-2) and plot in Fig. 8). The avalanche was triggered abruptly in which the powders slid down suddenly in a splashed manner, as shown in Fig. 4(c-3).

In the V_x profile, a higher positive velocity was spotted at the right hand side of the powder bed surface due to the lateral accumulation during continuous flow. Comparatively, the V_z profile was more indicative of the instantaneous potential conditions (Fig. 5). When COF = 0.1 (Fig. 5a), a gradual flow of powders clearly signalled that the high-rise powders were flowing downward under gravity, while low-rise powders were being pushed upward by rebound from the drum surface. With higher friction, the downward flow was shifted to the surface regions of the powder bed while the upward flow was shifted to the inner regions near the drum wall. When COF = 0.8 (Fig. 5c), the magnitude of V_z was higher than that of V_x, indicating the more dominating effect of gravity.

The velocity profiles of the sphere_EXP model are presented in Fig. 6 (V_x) and Fig. 7 (V_z). Compared to the sphere_mono model, sphere_EXP model presented similar powder flow characteristics (circular flow from the powder bed surface to the inner wall) and friction effects (hooded surface during gradually avalanche under low COF, and discontinued bed surface during abrupt avalanche under high COF). Nevertheless, due to more inner voids in the original static powder bed of sphere_EXP (Fig. 3g), the powders were prone to move and relocate these inner voids from the early stage of elevation, leading to an enhanced mobility (color bar in Fig. 6 and Fig. 7).

As shown in Fig. 8, at a low friction (COF < 0.4), sphere_EXP has a smaller AA value than sphere_mono due to the enhanced powder mobility, but both models showed a gradual avalanche flow. At a higher friction (COF > 0.5), both models presented an abrupt avalanche and a similar AA value. This finding shows that the AA is dependent on the size distribution during the gradual avalanche for the spherical models, but it is independent on the size distribution during the abrupt avalanche. The transition from gradual to abrupt avalanche was triggered by the variation of friction condition with a transient range of COF ≈ 0.4–0.5. This characteristic could be interpreted as a conversion of dominating driving force from friction-controlled gradual avalanche to the potential controlled abrupt avalanche, in agreement with the previous work by Chou et al. [14].

Here, we used sphere_EXP model to study the effects of different controlling factors in the RPA flow. Fig. 9 indicates that the effect of filling degree has a similar trend under different friction conditions. Our results show that the AA value is lower when the filling degree is <20%, but converged when the filling degree is higher than 25%. Clearly, a minimum threshold of filling degree, i.e., a minimum contact area to the drum wall, is required in order to have a consistent measurement of AA, which is consistent with previous studies [4,12,13]. Therefore, in our models, the filling degree was set as 28%.

Fig. 10 presents the effect of drum rotation speed. It is seen that the AA converged when the rotation speed was not higher than 0.3 rpm and was consistent under different friction conditions. It suggested that our adoption of 0.3 rpm was valid for both simulation and experiment. Based on our drum size and rotation speed used in the present work, the

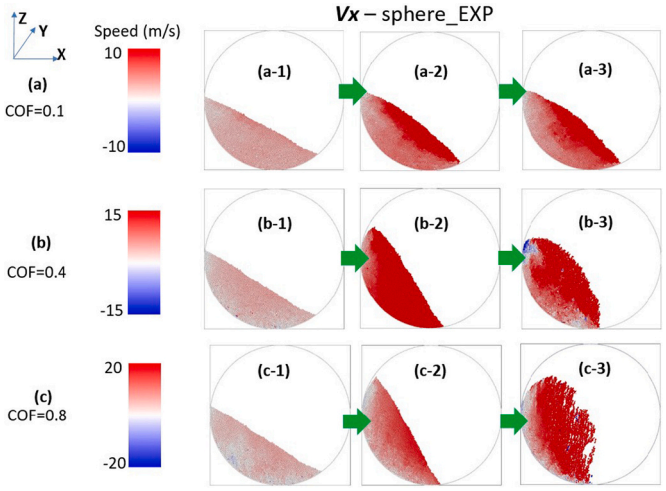

Fig. 6. Snapshots of V_x for sphere_EXP with different friction settings. The velocity is positive when its direction is along the forward direction axis, and vice versa.

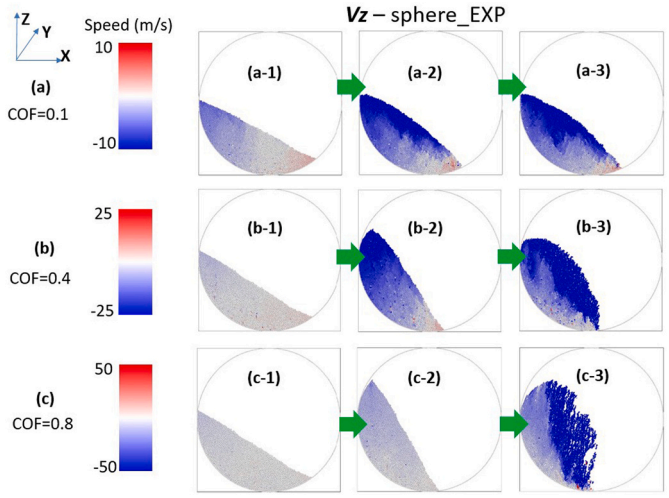

Fig. 7. Snapshots of V_z for sphere_EXP with different friction conditions. The velocity is positive when its direction is along the positive axis direction, and vice versa.

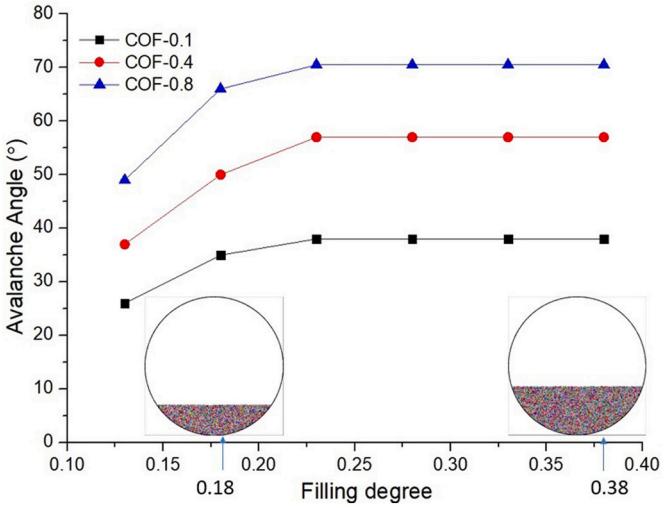

Fig. 9. Avalanche angle vs. filling degree under different COFs for sphere_EXP model. Two inserts showed the front views of models with 18% and 38% filling degree.

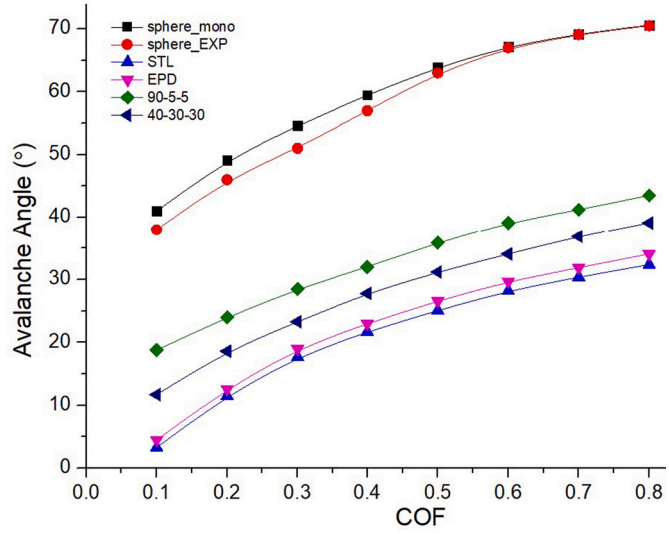

Fig. 8. Avalanche angle vs. COF for different types of powders.

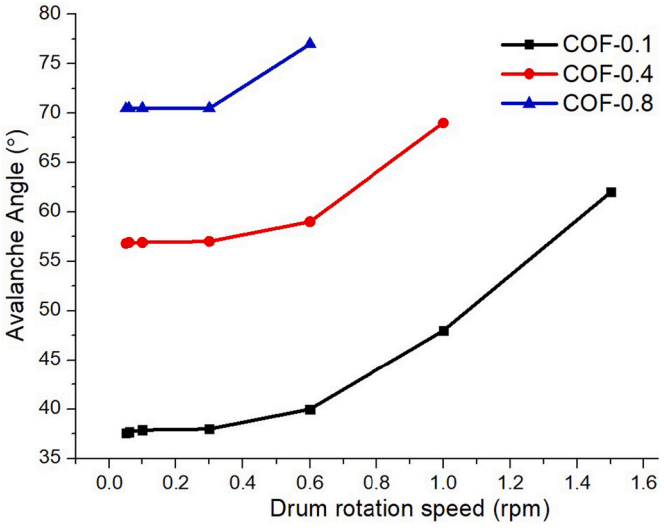

Fig. 10. Avalanche angle vs. drum rotation speed under different COFs for sphere_EXP model.

Froude number was found to be in the range of 0.0004–0.002 for a stable avalanche circulate flow pattern, which is consistent with a previous work (Mellmann 2001), in which the range of Froude number for a stable avalanche circulate flow was identified to be 0.0001–0.01. For the case of COF = 0.1, when the rotation speed exceeded 2 rpm, the powders would flow in a cataract manner without obvious avalanche, or even centrifuge along the inner wall under further increased drum rotation. Such effect of rapid drum rotation was also reported in previous works [4,32,33]. Furthermore, we found that a strong friction (COF ≥0.4) would trigger a cataract flow with a lower threshold of drum rotation speed, due to the enhanced hindrance to the flow motion. Thus, as shown in Fig. 10, we were only able to record AA under a slower drum rotation for COF = 0.4 and 0.8.

Besides the friction between two contacting powders, adhesion was also a concern because strong adhesion might agglomerate the powders and thereby affect the flow [15,68]. Here, we applied the JKR [69] method to describe inter-powder adhesion, whereby its formulation and parameters were reported in our previous work [62]. The variation of AA as a function of the adhesion energy is plotted in Fig. 11. It is seen that the AA increased parabolically with the introduction of adhesion, and the curve slope became linear after the adhesion energy exceeded 0.2 mJ/m^2. A similar trend was spotted for different friction conditions as COF = 0.1 or 0.4 (Fig. 11). In our simulations, when the adhesion energy was higher than 2 mJ/m^2, all the powders began to agglomerate into a big cluster and the individual powder flow vanished. Large powder clusters also formed with an even lower adhesion energy (~0.2 mJ/m^2) when COF = 0.8. Therefore, we didn't plot the AA curve for COF = 0.8.

3.2. Non-spherical models

As mentioned earlier, two types of non-spherical powders were created, that is, STL and EPD. Based on PF results (Fig. 3g), a lower PF corresponds to an increased amount of voids within the original static powder bed, leading to an early and intensified powder flow during rotational elevation. As shown in Fig. 8, the STL model with the lowest PF has the lowest AA too. The EPD model with the 2nd lowest PF exhibited a slightly higher AA than the STL model. With a mixture of different shapes, the 40:30:30 model showed a higher AA than the EPD

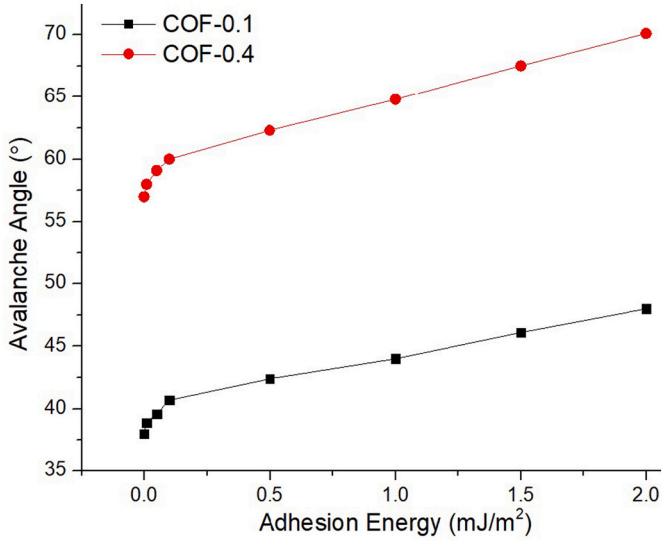

Fig. 11. Avalanche angle vs. adhesion energy with different COFs for sphere_EXP model.

model, but a lower AA than the 90:5:5 model. The AA vs COF plots as shown in Fig. 8 clearly indicates two separate zones between the spherical and non-spherical models, indicating the significance of the shape factor.

The velocity profiles for the 90:5:5 model are shown in Fig. 12 for $\boldsymbol{V_x}$ and Fig. 13 for $\boldsymbol{V_z}$. Compared to the pure spherical models, there were more voids in the original static packing bed, so that early and intensified powder movements became apparent. As shown in Fig. 12(a-1), most powders were in red color, indicating they were moving towards the right direction. However, there were a few blue-color powders inside the powder bed, which means they were moving in the opposite direction. With careful observation, we found that these "abnormal" powders were caused by the rolling motion of non-spherical powders. Compared to the spherical shape, the rolling of non-spheres had an increased disturbance onto the neighbouring powders in a wider ambient space. After collisions with the rolling non-spheres, some powders could gain instantaneous reverse velocities.

By tracking the rolling motion of individual non-spherical powders, we found that their rolling motion decreased tremendously with higher COFs. Under strong friction, powders were prone to agglomerate and

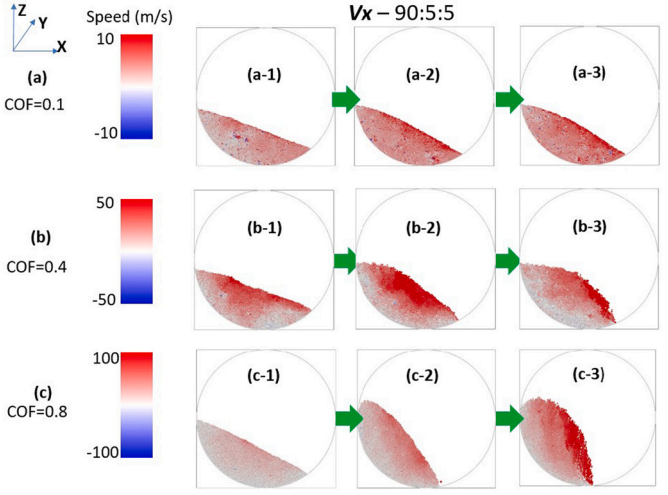

Fig. 12. Snapshots of $\boldsymbol{V_x}$ for the 90:5:5 model with different friction conditions. The velocity is positive when its direction is along the forward direction axis, and vice versa.

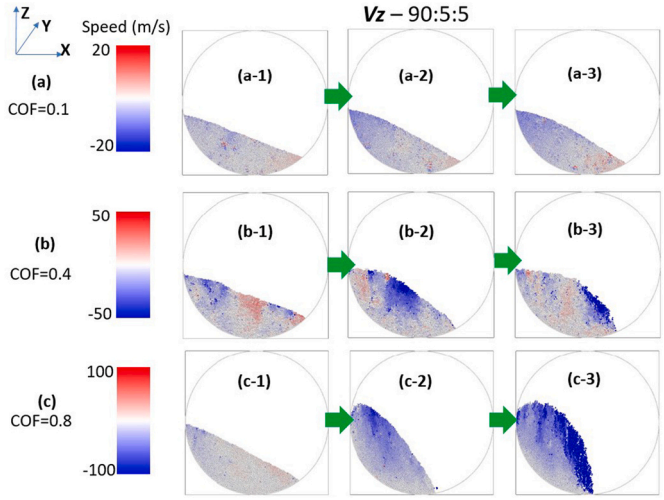

Fig. 13. Snapshots of $\boldsymbol{V_z}$ for the 90:5:5 model with different friction conditions. The velocity is positive when its direction is along the forward direction axis, and vice versa.

move as clusters, whose individual rolling motions were significantly retarded due to the interlocking with neighbouring clusters. As shown in the $\boldsymbol{V_z}$ plot (Fig. 13), when COF increased to 0.4 (Fig. 13b), different linear motions, such as falling (blue as downward motion) or rebounding (red as upward motion), appeared simultaneously among different clusters. Due to the formation of clusters, abrupt avalanches appeared, while the sphere_EXP model only showed abrupt avalanches when COF $>$ 0.5. When COF further increased to 0.8 (Fig. 13c), the entire powder bed elevated like a whole block, which crashed into individual powder flow pattern only by abrupt avalanche. Thus, the non-spheres caused strong disturbance to the powder flow under low friction, and became prone to abrupt avalanche with increasing friction.

As shown in Fig. 8, despite that the 90-5-5 model only constituted 10% of non-spherical powders, its AA values were only ~50% of those of sphere_EXP model. Therefore, the non-spherical shape imposed significant impact on the powder flow and triggered an early avalanche. Accordingly, the 40:30:30 model exhibited even lower AAs than the 90:5:5 model due to its lower content of spheres, but still higher AAs than the pure EPD model.

The effect of filling degree (Fig. 14), drum rotation speed (Fig. 15) and adhesion (Fig. 16) for the 90:5:5 model showed similar

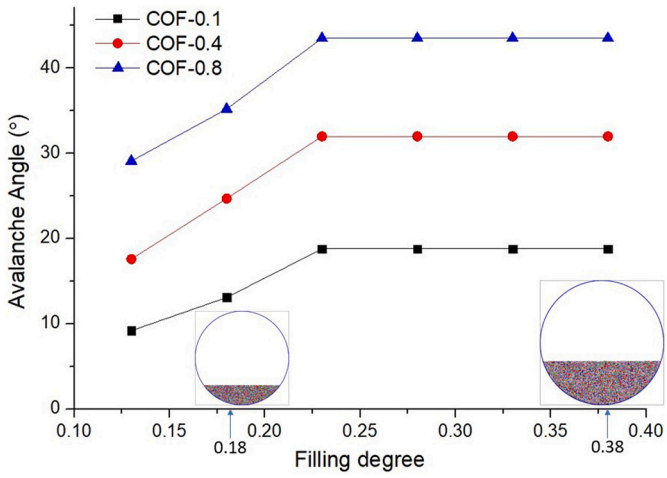

Fig. 14. Avalanche angle vs. filling degree under different COFs for the 90:5:5 model. The two inserts show the front view of the models with filling degree of 18% and 38%.

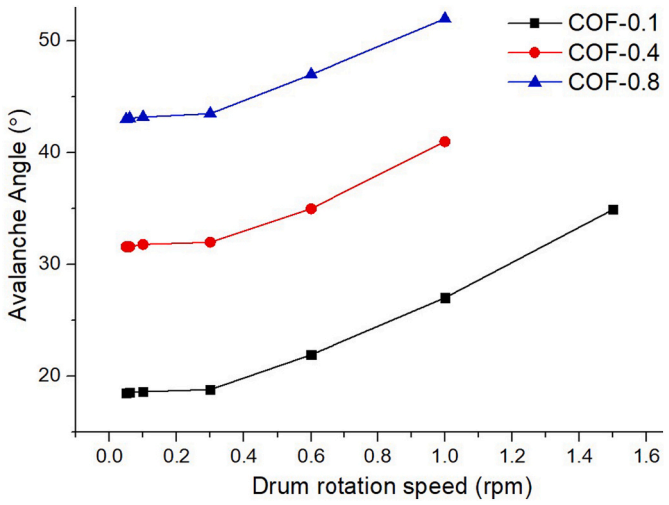

Fig. 15. Avalanche angle vs. drum rotation speed with different COFs for the 90:5:5 model.

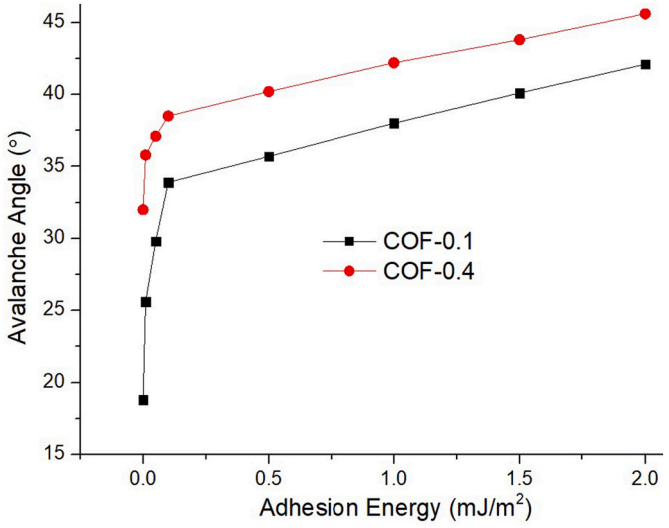

Fig. 16. Avalanche angle vs. adhesion energy with different COFs for the 90:5:5 model.

characteristics as those of sphere_EXP model (Figs. 9–11). It demonstrated that these factors had consistent effects to the powder flows. These results justified our choices of simulation parameters, in particular, a filling degree of 28% and a drum rotational speed of 0.3 rpm.

3.3. Extraction of COF and adhesion energy

In the above simulations, the values of COF and adhesion energy were varied over a wide range to perform a parametric study. Below, we would like to combine our DEM simulations and experimental measurements to determine the values of COF and adhesion energy for the powder used in this work.

In our previous Hall Flowmeter simulation with pure spherical powders [62], we used a guess-and-trial method to extract the representative values of $\mu_{pp\text{-}s}$ and $\mu_{pp\text{-}r}$ by combining DEM simulations and experimental measurements. Here, RPA test and Packing Fraction Characterization (PFC) were performed to extract the friction coefficients as well as the adhesion energy. The 90-5-5 model, which reflects the powder shapes used in our experiment, was chosen.

It is likely that, for the same powder material and surface roughness, the change in powder shape mainly alters the rolling COF but not the sliding COF. It is also expected that the change in shape can also affect the adhesion energy between powders. Since in our experiments, we used the same batch of powder for both previous Hall Flowmeter [62] and current RPA tests, the sliding friction coefficient $\mu_{pp\text{-}s}$, which is dependent on the powder surface roughness, was taken as the same value as before, which is $\mu_{pp\text{-}s} = 0.39$. Therefore, we focused on the extraction of the rolling friction coefficient $\mu_{pp\text{-}r}$, and the adhesion energy γ.

To extract the two physical quantities, we need two quantities from experimental output. Since the RPA test only provides the value of AA, we performed the PRC test by pouring powder into a PRC cup to provide the PFC value. The facility and procedure for measuring the PFC can be found in our previous work [62]. Schematic for the PFC measurement is shown in the inset chart in Fig. 17. The 90-5-5 powder model was used to simulate the PRC test.

Firstly, by fixing $\mu_{pp\text{-}s} = 0.39$, we carried out a series of RPA simulations by tuning $\mu_{pp\text{-}r}$ and γ to obtain different AA values, from which we extracted the combinations of $\mu_{pp\text{-}r}$ and γ values that gave rise to the experimental AA value of 41.3°, which are plotted as the black curve in Fig. 17. Similarly, the red curve stands for the combinations of $\mu_{pp\text{-}r}$ and γ values that satisfy the experimental PFC value of 0.58. As shown in Fig. 17, the cross-point of the two curves stands for the conditions that give rise to the experimental values for both AA and PFC as $\mu_{pp\text{-}r} = 0.37$ and $\gamma = 0.905$ mJ/m^2. Compared with the rolling COF of the spherical powders[52] (which is 0.51), inclusion of non-spherical shapes reduces the rolling COF. Furthermore, based on the effect of adhesion energy on the flow pattern, the value of 0.905 mJ/m^2 would give rise to a continuous flow, which is consistent with our experimental observation. It should be understood that these quantities are expected to be dependent on the powder size, shape and their distributions. Therefore, the extracted quantities might be considered as the average values of the powders used.

4. Conclusion

In conclusion, we carried out DEM simulations on RPA test to investigate the powder flow by focusing on the powder size, shape, friction and adhesion. By combining with experimental characterization, we extracted the physical quantities related to friction and adhesion. Our contributions and findings can be summarized as the

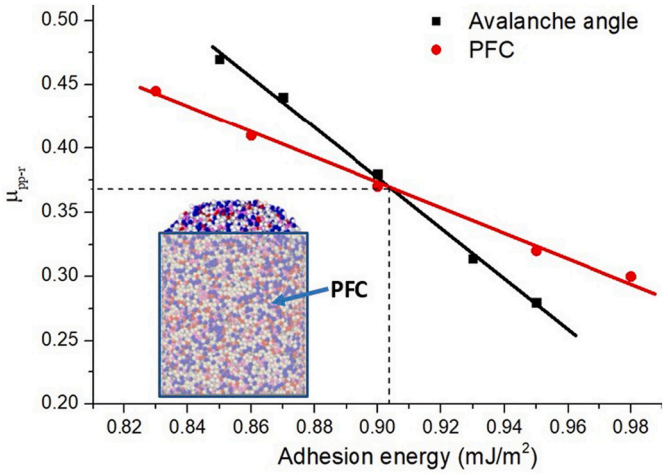

Fig. 17. Plots of rolling friction coefficient ($\mu_{pp\text{-}r}$) and adhesion energy (γ) that reproduced the experimental data of AA = 41.3° (black curve), and PFC = 58% (red curve). The cross-point gives rise to the intrinsic values of $\mu_{pp\text{-}r} = 0.37$ and $\gamma = 0.905$ mJ/m^2. The insert indicates the region for computing the PFC within the density cup. (For interpretation of the references to color in this figure legend, the reader is referred to the web version of this article.)

following:

1) A powder modelling scheme was introduced which included the effects of powder size and shape, especially that of the non-spherical powders.
2) A mixture of powders with different distribution of size and shape was considered to realistically reflect the powder used in experiments.
3) DEM simulations were performed by using different powder models to investigate the powder flow profiles and avalanche phenomena, and understand the effects of powder size, shape, friction and adhesion on the powder flowability and instability.
4) The effects of multiple factors, i.e., filling degree, drum rotation speed, adhesion energy, mixing ratio of spherical and non-spherical powders, were considered in relation to experimental measurements and a suitable regime for reliable measurements was identified.
5) The physical quantities related to friction and adhesion including non-spherical powders were extracted.

In summary, we presented a comprehensive DEM study on RPA tests. The in-depth understanding gained here in terms of powder packing and flowability can serve as a valuable benchmark for developing accurate CG models, as well as a useful reference for the fabrication of powder for additive manufacturing and powder metallurgy.

Credit author statement

L. Dai: Main contributor, DEM work, manuscript preparation.
Y.R. Chan: experimental work.
G. Vastola: Discussion, manuscript review, DEM code supporter.
Y.W. Zhang: Project leader, discussion, manuscript review.

Declaration of Competing Interest

The authors declare that they have no known competing financial interests or personal relationships that could have appeared to influence the work reported in this paper.

Data availability

No data was used for the research described in the article.

Acknowledgement

This work is funded by Agency for Science, Technology and Research (A*STAR) through grant A19E1a0097 ("Industrial Digital Design and Additive Manufacturing Workflows"). Y-WZ acknowledges the support from Singapore A*STAR SERC CRF Award.

Appendix A. Appendix

The Length and Width in Eq. (2) are schematized in Fig. A1. In Fig. A1(a) below, the major axis passes through the centre of mass of the object at an orientation corresponding to the minimum rotational energy of the shape. The minor axis passes through the centre of mass at right angle to the Major Axis. Then, in Fig. A1(b), the length (line-2) is defined as the longest projection on major axis (line-1) between two points on the perimeter. Similarly, in Fig. A1(c), the width (line-2) is defined as the longest projection on minor axis (line-1) between two points on the perimeter. By this means, it was guaranteed that width ≤length. Similar to the case of HS circularity, the value of Aspect ratio is 1 for a perfect sphere, and near 0 for a needle shape.

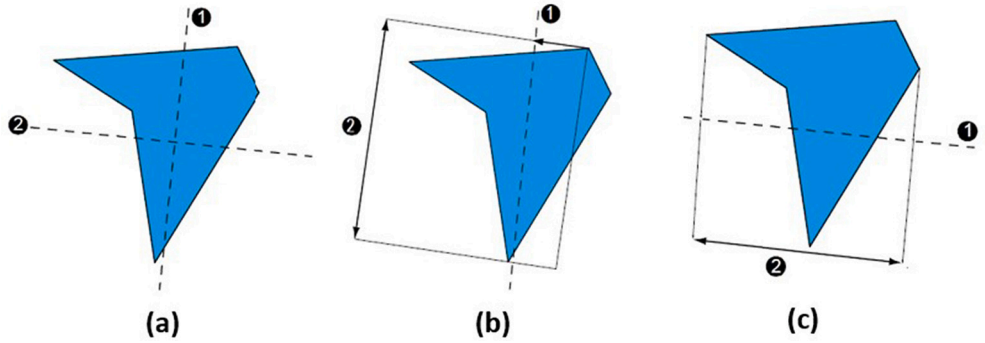

Fig. A1. (a) Major axis (line-1) and minor axis (line-2).
(b) Length (line-2) as the longest projection on major axis (line-1) between two perimeter points.
(c) Width (line-2) as the longest projection on minor axis (line-1) between two perimeter points.

References

[1] L.G. Ndiaye, S. Caillat, A. Chinnayya, D. Gambier, B. Baudoin, Application of the dynamic model of Saeman to an industrial rotary kiln incinerator: numerical and experimental results, Waste Manag. 30 (2010) 1188–1195.
[2] A.B. Spierings, M. Voegtlin, T. Bauer, K. Wegener, Powder Flowability characterisation methodology for powder-bed based metal additive manufacturing, Prog. Addit. Manuf. 1 (2016) 9–20.
[3] H.R. Norouzi, R. Zarghami, N. Mostoufi, Insights into the granular flow in rotating drums, Chem. Eng. Res. Des. 102 (2015) 12–25.
[4] J. Mellmann, The transverse motion of solids in rotating cylinders—forms of motion and transition behavior, Powder Technol. 118 (2001) 251–270.
[5] Z. Hu, X.Y. Liu, W.N. Wu, Study of the critical angles of granular material in rotary drums aimed for fast DEM model calibration, Powder Technol. 340 (2018) 563–569.
[6] L. Dai, V. Sorkin, G. Vastola, Y.W. Zhang, Dynamics calibration of particle sandpile packing characteristics via discrete element method, Powder Technol. 347 (2019) 220–226.
[7] S.C.D. Pont, R. Fischer, P. Gondret, B. Perrin, M. Rabaud, Instantaneous velocity profiles during granular avalanches, Phys. Rev. Lett. 94 (2005), 048003.
[8] D.A. Santos, M.A.S. Barrozo, C.R. Duarte, F. Weigler, J. Mellmann, Investigation of particle dynamics in a rotary drum by means of experiments and numerical simulations using DEM, Adv. Powder Technol. 27 (2016) 692–703.
[9] H. Yang, B.F. Zhang, R. Li, G. Zheng, V. Zivkovic, Particle dynamics in avalanche flow of irregular sand particles in the slumping regime of a rotating drum, Powder Technol. 311 (2017) 439–448.
[10] R. Han, J.Y. Feng, Y.F. Zhang, H. Yang, V. Zivkovic, R. Li, Numerical simulation of avalanche propagation dynamics in a rotating drum, Powder Technol. 380 (2021) 199–204.
[11] Y.F. Zhao, Y.J. Cui, Y. Hasebe, H.K. Bian, K. Yamanaka, K. Aoyagi, T. Hagisawa, A. Chiba, Controlling factors determining flowability of powders for additive manufacturing: a combined experimental and simulation study, Powder Technol. 393 (2021) 482–493.
[12] X.Y. Liu, E. Specht, J. Mellmann, Experimental study of the lower and upper angles of repose of granular materials in rotating drums, Powder Technol. 154 (2005) 125–131.

[13] S.H. Chou, S.S. Hsiau, Dynamic properties of immersed granular matter in different flow regimes in a rotating drum, Powder Technol. 226 (2012) 99–106.
[14] S.H. Chou, H.J. Hu, S.S. Hsiau, Investigation of friction effect on granular dynamic behavior in a rotating drum, Adv. Powder Technol. 27 (2016) 1912–1921.
[15] H. Yang, G.L. Jiang, H.Y. Saw, C. Davies, M.J. Biggs, V. Zivkovic, Granular dynamics of cohesive powders in a rotating drum as revealed by speckle visibility spectroscopy and synchronous measurement, Chem. Eng. Sci. 146 (2016) 1–9.
[16] Q. Chen, H. Yang, R. Li, W.Z. Xiu, R. Han, Q.C. Sun, V. Zivkovic, Compaction and dilatancy of irregular particles avalanche flow in rotating drum operated in slumping regime, Powder Technol. 364 (2020) 1039–1048.
[17] Q. Chen, R. Li, W.Z. Liu, G. Zheng, V. Zivkovic, H. Yang, Dynamics of irregular particles in the passive layer under the slumping regime, Powder Technol. 372 (2020) 32–39.
[18] Q. Chen, H. Yang, R. Li, G. Zheng, P. Kong, Rearrangement of irregular sand particles in a rotary drum after avalanche flow, Powder Technol. 360 (2020) 549–554.
[19] P. Richard, N. Taberlet, Recent advances in DEM simulations of grains in a rotating drum, Soft Matter 4 (2008) 1345–1348.
[20] C.J. Coetzee, Calibration of the discrete element method and the effect of particle shape, Powder Technol. 297 (2016) 50–70.
[21] C.J. Coetzee, Review: calibration of the discrete element method, Powder Technol. 310 (2017) 104–142.
[22] C.J. Coetzee, Particle upscaling: calibration and validation of the discrete element method, Powder Technol. 344 (2019) 487–503.
[23] C. Coetzee, Calibration of the discrete element method: strategies for spherical and non-spherical particles, Powder Technol. 364 (2020) 851–878.
[24] M. Combarros, H.J. Feise, H. Zetzener, A. Kwade, Segregation of particulate solids: experiments and DEM simulations, Particuology 12 (2014) 25–32.
[25] S.L. Yang, Y.H. Sun, L.Q. Zhang, J.W. Chew, Segregation dynamics of a binary-size mixture in a three-dimensional rotating drum, Chem. Eng. Sci. 172 (2017) 652–666.
[26] F.H. Yu, S. Zhang, G.Z. Zhou, Y. Zhang, W. Ge, Geometrically exact discrete-element-method (DEM) simulation on the flow and mixing of sphero-cylinders in horizontal drums, Powder Technol. 336 (2018) 415–425.
[27] T. Barczi, M. Kohout, M. Kozakovic, J. Havlica, C. Ratnayake, Discrete element method simulation and experimental validation of pattern development in a rotating drum mixer, Chem. Eng. Technol. 41 (2018) 1524–1530.
[28] N. Gui, J. Yan, W.K. Xu, L. Ge, D.L. Wu, Z.L. Ji, J.S. Gao, S.Y. Jiang, X.T. Yang, DEM simulation and analysis of particle mixing and heat conduction in a rotating drum, Chem. Eng. Sci. 97 (2013) 225–234.
[29] X.W. Xiao, Y.Q. Tan, H. Zhang, R. Deng, S.Q. Jiang, Experimental and DEM studies on the particle mixing performance in rotating drums: effect of area ratio, Powder Technol. 314 (2017) 182–194.
[30] S.Y. Liu, Z. Hu, W.N. Wu, J.S. Zhan, F.B. Herz, E. Specht, DEM study on the surface mixing and whole mixing of granular materials in rotary drums, Powder Technol. 315 (2017) 438.
[31] D. Li, X. Xu, J.H. Chen, K. Yang, X.L. Liu, L. Yang, Numerical study on the effect of drum on the flow behavior of binary-size particles in rotating drums, Powder Technol. 386 (2021) 108–119.
[32] R.Y. Yang, R.P. Zou, A.B. Yu, Microdynamic analysis of particle flow in a horizontal rotating drum, Powder Technol. 130 (2003) 138–146.
[33] R.Y. Yang, A.B. Yu, L. McElroy, J. Bao, Numerical simulation of particle dynamics in different flowregimes in a rotating drum, Powder Technol. 188 (2008) 170–177.
[34] V. Salinas, C. Quininao, S. Gonzalez, G. Castillo, Triggering avalanches by transverse perturbations in a rotating drum, Sci. Rep. 11 (2021) 13936.
[35] J.H. Kasper, V. Magnaimo, S.D.M.D. Jong, A. Beek, A. Jarray, Effect of viscosity on the avalanche dynamics and flow transition of wet granular matter, Particuology 59 (2021) 64–75.
[36] P.A. Langston, M.A. Al-Awamleh, F.Y. Fraige, B.N. Asmar, Distinct element modelling of non-spherical frictionless particle flow, Chem. Eng. Sci. 59 (2004) 425–435.
[37] K.J. Dong, C.C. Wang, A.B. Yu, A novel method based on orientation discretization for discrete element modeling of non-spherical particles, Chem. Eng. Sci. 126 (2015) 500–516.
[38] W.Q. Zhong, A.B. Yu, X.J. Liu, Z.B. Tong, H. Zhang, DEM/CFD-DEM modelling of non-spherical particulate systems: theoretical developments and applications, Powder Technol. 302 (2016) 108–152.
[39] H. Kruggel-Emden, S. Rickelt, S. Wirtz, V. Scherer, A study on the validity of the multi-sphere discrete element method, Powder Technol. 188 (2008) 153–165.
[40] M. Kodam, R. Bharadwaj, J. Curtis, B. Hancock, C. Wassgren, Force model considerations for glued-sphere discrete element method simulations, Chem. Eng. Sci. 64 (2009) 3466–3475.
[41] C.Q. Li, W.J. Xu, Q.S. Meng, Multi-sphere approximation of real particles for DEM simulation based on a modified greedy heuristic algorithm, Powder Technol. 286 (2015) 478.
[42] B. Soltanbeigi, A. Podlozhnyuk, S.A. Papanicolopulos, C. Kloss, S. Pirker, J.Y. Ooi, DEM study of mechanical characteristics of multi-spherical and superquadric particles at micro and macro scales, Powder Technol. 329 (2018) 288–303.
[43] Y. You, Y.Z. Zhao, Discrete ement modelling of ellipsoidal particles using super-ellipsoids and multi-spheres: a comparative study, Powder Technol. 331 (2018) 179–191.
[44] J. Pachon-Morales, P. Perre, J. Casalinho, H. Do, D. Schott, F. Puel, J. Colin, Potential of DEM for investigation of non-consolidated flow of cohesive and elongated biomass particles, Adv. Powder Technol. 31 (2020) 1500–1515.
[45] D. Queteschiner, T. Lichtenegger, S. Peiker, S. Schniderbrauer, Multi-level coarse-grain model of the DEM, Powder Technol. 338 (2018) 614–624.
[46] D.S. Nasato, R.Q. Albuquerque, H. Briesen, Predicting the behavior of granules of complex shapes using coarse-grained particles and artificial neural networks, Powder Technol. 383 (2021) 328–335.
[47] T. De, J. Chakraborty, J. Kumar, A. Tripathi, M. Sen, W. Ketterhange, A particle location based multi-level coarse-graining technique for discrete element method (DEM) simulation, Powder Technol. 398 (2022), 117508.
[48] D. Dudzinski, A. Devillez, A. Moufki, D. Larrouquere, V. Zerrouki, J. Vigneau, A review of developments towards dry and high speed machining of Inconel 718 alloy, Int J Mach Tool Manu 44 (2004) 439–456.
[49] K.N. Amato, S.M. Gaytan, L.E. Murr, E. Martinez, P.W. Shindo, J. Hernandez, S. Collins, F. Medina, Microstructures and mechanical behavior of inconel 718 fabricated by selective laser melting, Acta Mater. 60 (2012) 2229–2239.
[50] Q.B. Nguyen, M.L.S. Nai, Z.G. Zhu, C.N. Sun, J. Wei, W. Zhou, Characteristics of Inconel powders for powder-bed additive manufacturing, Eng. 3 (2017) 695–700.
[51] GE additive. https://www.ge.com/additive/.
[52] W.C. Xia, Role of particle shape in the floatability of mineral particle: an overview of recent advances, Powder Technol. 317 (2017) 104–116.
[53] J.Y. Zhu, Y.Y. Liang, Y.H. Zhou, The effect of the particle aspect ratio on the pressure at the bottom of sandpiles, Powder Technol. 234 (2013) 37–45.
[54] R.D. Hryciw, M. Asce, J.X. Zheng, S.M. Asce, K. Shetler, S.M. Asce, Particle roundness and sphericity from images of assemblies by chart estimates and computer methods, J. Geotech. Geoenviron. Eng. 142 (2016) 04016038.
[55] I. Cruz-Matias, D. Ayala, D. Hiller, S. Gutsch, M. Zacharias, S. Estrade, F. Peiro, Sphericity and roundness computation for particles usingthe extreme vertices model, J. Comput. Sci. 30 (2019) 28–40.
[56] J.K. Mitchell, K. Soga, Fundamentals of Soil Behavior, 3rd edition, John Wiley & Sons, Hoboken, 2005.
[57] T. Roussillon, H. Piegay, I. Sivignon, L. Tougne, F. Lavigne, Automatic computation of pebble roundness using digital imagery and discrete geometry, Comput. Geosci. 35 (2009) 1992–2000.
[58] https://www.mercuryscientific.com/homepage.
[59] A.D. Renzo, F.P.D. Maio, Comparison of contact-force models for the simulation of collisions in DEM-based granular flow codes, Chem. Eng. Sci. 59 (2004) 525–541.
[60] A.D. Renzo, F.P.D. Maio, An improved integral non-linear model for the contact of particles in distinct element simulations, Chem. Eng. Sci. 60 (2005) 1303–1312.
[61] J. Ai, J.F. Chen, J.M. Rotter, J.Y. Ooi, Assessment of rolling resistance models in discrete element simulations, Powder Technol. 206 (2011) 269–282.
[62] L. Dai, Y.R. Chan, G. Vastola, N. Khan, S. Raghavan, Y.W. Zhang, Characterizing the intrinsic properties of powder – a combined discrete element analysis and hall flowmeter testing study, Adv. Powder Technol. 32 (2021) 80–87.
[63] D.A. Weitz, Packing in the spheres, Science 303 (2004) 968–969.
[64] A. Mehta, G.C. Barker, The dynamics of sand, Rep. Prog. Phys. 57 (1994) 383–416.
[65] R.T. Fowler, F.A. Wyatt, The effect of moisture content on the angle of repose of granular solids, Aust. J. Chem. Eng. (1960) 5–8.
[66] X.Y. Liu, E. Specht, J. Mellmann, Slumping-rolling transition of granular solids in rotary kilns, Chem. Eng. Sci. 60 (2005) 3629–3636.
[67] C.M. Dury, G.H. Ristow, Boundary effects on the angle of repose in rotating cylinders, Phys. Rev. E 57 (1998) 4491–4497.
[68] X.L. Deng, J.V. Scicolone, R.N. Dave, Discrete element method simulation of cohesive particles mixing under magnetically assisted impaction, Powder Technol. 243 (2013) 96–109.
[69] K.L. Johnson, K. Kendall, A.D. Roberts, Surface energy and the contact of elastic solids, Proc. R. Soc. Lond. A 324 (1971) 301–313.